Morphological changes and segregation of β-$Al_9Fe_2Si_2$ phase: A perspective from better recyclability of cast Al-Si alloys

C. B. Basak*, N. Hari Babu

BCAST, Brunel University London, Kingston Lane, Uxbridge, Middlesex UB8 3PH, UK

Abstract

High iron impurity has detrimental effects on the castability and tensile properties of recycled aluminium alloys. The present study reports the engineering of intermetallic β-phase present in hypoeutectic cast Al-Si model alloy systems with high Fe content (2wt% Fe) in order to demonstrate the promising recyclability despite having high Fe content. Thermodynamic interplay between Si and Fe concentration on the formation of the β-phase and the solidification behaviour of the hypoeutectic Al-Si alloys has been explored. It has been demonstrated that with suitable heat treatment it is possible to alter the morphology of the β-phase and based on the experimental evidences, for the first time, the mechanism behind the solid-state morphological changes of beta phase has been proposed. Based on the experimental results and thermodynamic calculations it has been suggested that elimination of beta phase by gravitational segregation is more suitable for the near-eutectic 10wt% Si alloy; whereas for 6wt%Si alloy, morphological change of β-phase is recommended. It was also found that morphological change of beta-phase and Si could help recovering the strength and ductility in the recycled Al-Si alloys having high Fe content.

Keywords

Aluminium alloy; intermetallics; precipitation; thermodynamic modelling; scanning electron microscopy

* Corresponding author: chandrabhanu.basak@brunel.ac.uk (C. B. Basak)

1. Introduction

Primary production of aluminium from bauxite ore attracts an energy expenditure of about 186 MJ/kg of metallic aluminium; however, this expenditure could be reduced to 10–20 MJ/kg by recycling the discarded aluminium products or scraps [1, 2]. These figures emphasize not only the economic importance but also the underlying environmental benefits in the favour of recycling aluminium scraps. Recyclable scrap may come from manufacturing industries, automobile sector, beverage cans and from other miscellaneous sources. Because of the diversified sources and involvement of processing equipment the recycled aluminium accumulates several metallic impurities, e.g. Si, Mg, Ni, Zn, Pb, Cr, Fe, Cu, V, Mn to name a few. Different physical separation techniques are being employed in the industries today before melting the Al-scraps to minimize the impurity pick up in the recycled aluminium products; e.g. magnetic separation, air separation, heavy media separation (using water based slurry) and colour sorting [3]. Despite employing such physical separation techniques the residual iron impurity poses as the major challenge for the recycled aluminium because of two main reasons. Firstly, higher iron content usually associated with less flowability and shrinkage porosities in the casting i.e. poor castability and secondly, it drastically reduces the ductility due to the formation of intermetallic phases, specifically the β-phase.

Al-Si alloys are usually considered as cast alloys and have applications in automobile sectors. Higher iron content in Al-Si alloy system causes formation of several intermetallic phases, e.g. hexagonal α-Al_8Fe_2Si (τ_5), monoclinic β-$Al_9Fe_2Si_2$ (τ_6), δ-Al_4Fe_2Si (τ_{11}) etc. along with other binary Al-Fe compounds ($Al_{13}Fe_4$, Al_5Fe_2 etc.); further details on these intermetallic compounds are available in the literatures [4-7]. However, thermodynamic selection of intermetallic phase formation is strongly dependent on the concentration of both Fe and Si [8]. For example, at a temperature of 625 ^{o}C in Al-6wt% Si-2wt% Fe alloy only α-Al_8Fe_2Si

and liquid can coexist, however, increasing Si content to 10wt% would cause equilibrium between β-$Al_9Fe_2Si_2$ phase and liquid at the same temperature.

Two model alloys have been considered in the present study; namely, Al-6wt% Si-2wt% Fe and Al-10wt%Si-2wt%Fe mimicking high iron bearing recycled Al-Si cast alloy. Choice of two alloys would also enable one to understand the role of the silicon in these high Fe content alloys. In these alloys the relevant intermetallic phase present at room temperature is the so called β-$Al_9Fe_2Si_2$, also designated as β-Al_5FeSi or τ_6 phase in the literatures [4- 8]. It is known that this inherently brittle β-phase is formed as three-dimensionally interlinked thin platelets with characteristic needle-like appearance in the micrographs [9, 10]. This interconnectivity of the β-phase alongwith its poor thermal conductivity causes retention of isolated liquid metal pool in the inter-dendritic cavities causing shrinkage porosity in the final casting upon solidification [11]. Higher Fe content in the Al-Si alloys also causes reduced fluidity of the molten alloy causing inefficient and rather poor die filling [12]. These factors together render poor castability in high-Fe Al-Si alloys as mentioned earlier. On the other hand, the sharp corners (and incoherent interface) of the β-phase act as stress concentrators in the matrix causing severe brittleness in the final casting; with no more than about 2% ductility [13]. The only apparent advantage of having higher Fe content (upto about 1.5wt%Fe) is the avoidance of die sticking or soldering in the die castable Al-Si-Fe alloys [**Error! Bookmark not defined.**].

2. Managing higher Fe content

Different approaches exist on how to tackle the high iron content in the recycled aluminium alloy. Most straightforward approach to counter the level of iron impurity is to dilute the recycled aluminium using primary aluminium; also known as “down cycling” [3]. Second approach is to hinder the formation of β-phase by Mn addition, in case of moderate Fe level,

by promoting the formation of $Al_{15}(Fe, Mn)_3Si_2$ phase having polygonal morphology. Such change in morphology actually improves the ductility of the castings. However, beyond about 1.2 wt% Fe both needle like β-phase and polygonal $Al_{15}(Fe, Mn)_3Si_2$ phase appears which diminishes the positive effect of Mn addition [**Error! Bookmark not defined.**]. The question remains to be answered and will be dealt in this paper is, if one accommodate more than 1.2wt%Fe concentration in recycled Al-Si cast alloy without Mn addition.

In Al-Si alloys almost all Fe contributes to the formation of equilibrium β-phase (i.e. higher Fe causes more phase fraction of β-phase) owing to its extremely low solid solubility in Al of about 10ppm [14]. Therefore, it makes sense that rather than focusing on Fe if one diverts the focus on dealing with the β-phase it could offer some indirect way to deal with the high Fe content in Al-Si alloys. Two different methodologies could be thought based on this philosophy; namely, gravitational segregation of β-phase and alteration of morphology of the β-phase.

Segregation of β-phase in liquid alloy is possible owing to the difference in the density between the β-phase and liquid-Al; which will be discussed in details later on. It is to be noted that segregation of β-phase changes the overall chemistry of the liquid alloy towards low iron and low silicon content; whereas alteration of morphology of the β-phase targets to keep the chemistry invariant and yet improving the mechanical properties. It is but natural that segregation of β-phase can only take place before the final casting is produced; whereas altering the morphology of β-phase can be done in the final cast product using suitable heat-treatment. Along the similar line of thought, one could use filtration technique as well to separate the β-phase from the molten liquid [15]. Based on the theoretical calculations and experimental observations further discussions will be carried out in the light of the above philosophy in the rest of this article.

3. Experimental procedure

Two model alloys were selected for the present study, as mentioned earlier, Al-6wt%Si-2wt%Fe and Al-10wt%Si-2wt%Fe alloy; for the sake of brevity these two alloy would be referred as 6Si and 10Si, respectively, in the rest of the article. Al ingots (from Norton Aluminium Ltd.), Al-50wt%Si and Al-45wt%Fe master alloys (both from KBM Affilips) having commercial purity level were used for preparing the alloy. A resistance furnace and boron nitride coated clay bonded graphite crucible was used for preparing the alloy. First Al ingot was melt and then Al-Si and Al-Fe master alloy was added sequentially with stirring. A melt of about 500 g was prepared at 800 ^{o}C with intermittent stirring of at least 6 times with a total holding time of 2 hour at that temperature to ensure chemical homogeneity. Commercially available degassing tablet was used and the top oxide layer of the melt was skimmed off. Finally, the melt at a temperature of 750 ^{o}C was poured into a boron nitride coated mild steel cylindrical die of 25 mm in diameter preheated at 250 ^{o}C. An average cooling rate of about 4- 5 ^{o}C/s is expected based on previous experiments and is also supported by existing literature [**Error! Bookmark not defined.**]. A part of the melt also poured in a 60 mm dia. steel die for chemical analysis using glow discharge optical emission spectroscopy (GD-OES). GD-OES chemical analysis is provided at table 1, which is averaged over five analyses from five random locations.

For microstructural analysis, standard metallographic practice was adopted where final polishing was carried out using 0.25 μm colloidal silica. Aqueous solution of 10 wt% NaOH was used for chemical etching, whenever required. A field emission scanning electron microscope (FESEM) (having both secondary electron (SE) and back scattered electron (BSE) detectors) equipped with energy dispersive spectroscope (EDS) was used for microstructural analysis. X-ray diffractometer was equipped with solid-state detector and operated at 1.6 kW Cu-K_{α} radiation. Thermodynamic calculations were performed with

CALculation of PHAse Diagram (CALPHAD) methodology using PandaT software [16] and image analysis were carried out using ImageJ software [17]. Tensile testing was carried out in selected specimens with 25 mm gauge length in compliance with ASTM B557-10 standard [18].

4. Results and discussions

Fig. 1 (a) and (b) are the as-cast microstructure of 6Si and 10Si samples (in as polished condition) in back scattered electron mode where β-phase appears brighter due to the presence of heavy element like Fe. Fig. 2 (a) shows magnified view of a shrinkage porosity in the sample due to the presence of β-phase as discussed in the introduction. Fig. 2 (b) is yet another SEM micrograph of deeply etched sample where complex shape of the β-phase is partially revealed. Eutectic Si in Al matrix and presence of Fe in β-$Al_9Si_2Fe_2$ phase can be detected under x-ray mapping using EDS; as shown in fig. 3 (a-c).

4.1 Thermodynamic calculations

The free energy of mixing of any given phase in Al-Fe-Si system can be written as –

$$G_m^{\emptyset} = G^0 + G^{id} + G^{xs} \quad (1)$$

$$G^0 = {x_{Al}}^0 G_{Al}^{\emptyset} + {x_{Si}}^0 G_{Si}^{\emptyset} + {x_{Fe}}^0 G_{Fe}^{\emptyset} \quad (2)$$

$$G^{id} = RT(x_{Al} \ln x_{Al} + x_{Si} \ln x_{Si} + x_{Fe} \ln x_{Fe}) \quad (3)$$

Where, subscript *m* stands for mixing for the phase Φ; and all these equations are generic in nature. The terms on the left hand side of the equation (1) stand for Gibbs free energy for mechanical mixture, ideal solution and excess, respectively. Gibbs free energy of mechanical mixture (G^0) and Gibbs free energy for ideal solution (G^{id}) are expressed as per equation (2) and (3) in terms of the mole fraction (x) of the constituent (i.e. Al, Fe or Si) . Usually the standard element reference (SER) state is used as the reference state (i.e. the stable structure of the element at 25 °C and 1 bar) of Gibbs energy [19]. The excess Gibbs free energy (G^{xs})

can be expressed mathematically in different way depending on the type of phase being modelled. For the disordered/solution phases (e.g. liquid, Al or Si) G^{xs} can be expressed by the regular solution model as follows –

$$G^{xs} = x_{Al}x_{Si}L^{\emptyset}_{Al,Si} + x_{Fe}x_{Si}L^{\emptyset}_{Fe,Si} + x_{Al}x_{Fe}L^{\emptyset}_{Al,Fe} + x_{Al}x_{Si}x_{Fe}L^{\emptyset}_{Al,Si,Fe} \quad (4)$$

where, the terms L are the binary and ternary interaction parameters denoted by the subscript. Often these interaction terms can be expressed in the so-called Redlich-Kister form –

$$L^{\emptyset}{}_{A,B} = \sum_{i=0}^{n} l_i (x_A - x_B)^i \quad (5)$$

The coefficients l_i are usually expressed as the polynomial of temperature –

$$l_i = \sum_{j=0}^{m} q_j T^j \quad (6)$$

Where, the coefficients q_j are the pure numeric values that are optimized with the aid of experimental data. It is worth noting that eqn. (4) to (6) are applicable only for disordered phases and it is usual to apply sub-lattice model for the intermetallic phases described elsewhere in the literature [20]. Once such thermodynamic optimization is done then the Gibbs free energy of individual phase can be calculated at any given temperature and alloy composition and equilibrium condition between two or more phases can be established by minimizing the free energy of the system; as follows –

$$G = \sum_{\emptyset=0}^{p} x_{\emptyset} G^{\emptyset}_{m} \quad (7)$$

Where, p is the number of the phases participating in the equilibrium. The foregoing discussion is a brief account of the so-called CALPHAD methodology. Present thermodynamic calculations were carried out using commercially available aluminium alloy database by CompuTherm LLC [**Error! Bookmark not defined.**].

The calculated isopleth at 2 wt% Fe obtained from CALPHAD calculation is depicted in fig. 4; where 6Si and 10Si compositions are indicated. It is to be noted that though lever rule can not be applied in an isopleth but an isopleth is helpful in determining the phases present at any given temperature and composition. For example, it could be seen from fig. 4 that during

the early stage of solidification in 6Si alloy α-phase is involved, which is absent in 10Si alloy. Fig. 5 (a) represents the yield of β-phase in the composition space of Si and Fe at eutectic temperature (575.7 ^{o}C). Projection of fig. 5 (a) generates fig. 5 (b) in Si-Fe composition space showing different regions which can be expressed using the following inequalities -

$$w_{Si} < 0.27w_{Fe} + 0.512 \quad (8)$$

$$0.27w_{Fe} + 0.512 \leq w_{Si} \leq 0.525w_{Fe} + 0.508 \quad (9)$$

$$w_{Si} > 0.525w_{Fe} + 0.508 \quad (10)$$

In a Al-Fe-Si alloy, for any given wt%Fe (w_{Fe}) if the Si content in the alloy satisfies the inequality (8) then formation of β-phase is thermodynamically not possible, if it follows inequality (10) then amount of β-phase is independent of Si content. For any other value of Si content, the β-phase fraction is dependent on both Si and Fe.

Fig. 6 (a) and (b) show solidification profile for 6Si and 10Si using both Scheil and equilibrium solidification model; whereas fig. 6 (c) is the comparative yield of β-phase between 6Si and 10Si samples. It is interesting to note that the calculated liquid phase fraction does not differ in any appreciable way between the two solidification models for a given alloy, especially for 10Si. The reason for such model invariant solidification is due to the fact, as can be seen from fig. 4, that the liquid phase is in equilibrium with one of the intermetallic phases; namely, α-phase and/or β-phase. Since, these intermetallic phases do not show appreciable range of solute solubility for either Si or Fe. Therefore, as solidification progresses the fraction of intermetallic phase (β or α-phase) increases without any appreciable change in its composition; as exhibits by equilibrium model or Scheil model. Therefore, the corresponding liquid phase fraction also remains model invariant at any given temperature. Only small deviation occurs between the two models due to the generation of pro-eutectic Al having appreciable solubility of Si. Thus, such variation is slightly more predominant where pro-eutectic Al is more, i.e. for 6Si alloy, as can be seen from fig. 6 (a).

It is worth noting that the formation of β-phase can be divided into primary and secondary stage; the former is indicated when it forms above eutectic point (see fig. 6 (c)). Primary β-phase can form in low Si alloy (e.g. 6Si) by U-type quasi-peritectic reaction; $L + \alpha \leftrightarrow (Al) + \beta$, followed by the precipitation from the liquid as solidification progresses (for both 6Si and 10Si); perhaps by the growth of the existing beta platelets. Naturally, one can expect longer and coarser platelets of beta as shown in fig. 1 (b). At the end of solidification, β-phase forms via eutectic reaction ($L \leftrightarrow (Al) + (Si) + \beta$) at 575.7 ^{o}C for both 6Si and 10Si as can be seen from fig. 6 (a-b). The resultant β-phase is expected to be finer than the primary β-phase similar to fig. 1 (a).

4.2 Gravitational segregation of β-phase

The calculated eutectic temperature was found to be at 575.7 ^{o}C, which is almost identical as that of Al-Si binary eutectic temperature. This clearly suggests that Fe does not affect the basic Al-Si chemical interaction and almost all Fe is converted into either α-phase or β-phase; validating the philosophy of phase segregation as a means of iron removal as stated earlier.

From fig. 6 (b) it can be seen that for 10Si alloy, at 600 ^{o}C, the liquid composition is 9.7wt% Si- 0.9wt% Fe which is in equilibrium with β-phase (phase fraction of 3.6% mole/mole). This liquid-solid two-phase equilibrium is best suited for gravitational segregation. In fact, when 10Si alloy sample was treated at 600 ^{o}C for just 2 hour it causes severe gravitational segregation visible in unaided human eye, as shown in the fig. 7 (a). Image analysis results showing change in aspect ratio of β-phase are presented in fig. 7 (b). This clearly shows that during gravitational segregation the aspect ratio of β-phase also decreases suggesting morphological change. The x-ray trace from top and bottom surface of this sample could be compared along with the as-cast sample, as shown in the fig. 7 (c), to appreciate the extent of segregation of β-phase. The secondary electron along with the back-scattered electron micrographs of the entire cross section of 10Si sample held at 600 ^{o}C for 2 hour is presented

in the fig. 8. The SEM micrograph alongwith x-ray mapping of the bottom surface of the segregated sample exhibit high density of β-phase particles as presented in the fig. 9 (a-c). The growth of β-phase particles is remarkable when compared with the as-cast samples. The shape of β-phase also changes from interconnected flake like structure in as-cast sample to a less complex blocky prismatic particle in segregated condition. It is worthwhile to mention here that the chemistry of the β-phase does not change much from the cast sample to this segregated sample. However, based on the 10 random measurements with EDS it could be seen that exposure at 600 ^{o}C temperature for 24 hour slightly increases the iron content of the β-phase. The chemical compositions of the β-phases are presented in table 2 under different heat-treatment conditions. It is interesting to see from table 2 that with increase in Fe corresponding decrease in Al and Si content take place with an approximate atomic ratio of 1:2. Further experimental evidences are required to conclude the chemical change in the β-phase as a function of time and temperature.

It is known that for as-cast aluminium alloy microstructural features, especially, size and shapes of intermetallic phases vary across the cross section [**Error! Bookmark not defined.**, 21]. From the image analysis results of as-cast 10Si sample the area fraction of the β-phase was found to be around 11.2%, 8.8% and 7.9% from the edge to centre giving an average value of 9.3%. Whereas the same from the bottom surface 10Si sample exposed at 600 ^{o}C for 2 hour is about 9.4%. Since, the area fraction does not change significantly from the as-cast sample, it could be understood that the coarsening and segregation of the β-phase takes place without appreciable change in phase volume. It is interesting to observe that the top surface of segregated sample (600 ^{o}C for 2 hour) still shows some fine needles β-phase (area fraction of about 0.015) which forms during the solidification of the remaining liquid (with 0.9 wt% Fe) in thermodynamic equilibrium with the β-phase at 600 ^{o}C.

Taking the densities of liquid Al and the β-phase into consideration one can invoke Stokes law to calculate the terminal velocity of the segregating β-phase particles. Similar calculation has already been performed by Sabestari et. al. for Al-12.5 wt% Si-1.2 wt% Fe alloy at 630 ^{o}C in laminar flow regime [22]. It is worthwhile to recall the equation of the velocity from a free-body diagram of a particle –

$$V_p\rho_p\frac{dv}{dt} = V_p\rho_p g - V_p\rho_l g - \frac{1}{2}\rho_l A_p C_D v^2 \qquad (11)$$

Where, subscript p and l stand for particle and liquid, ρ density, V volume, v velocity, t time, gravitational acceleration g, A is projected area and C_D is the drag coefficient. Left hand term is the net force acting on a particle (mass multiplied by acceleration); first and second terms on the right hand side are gravitational and buoyancy force respectively and the last term is the drag force. When net force on the particle is zero, the equation (11) can be simplified to the following equation describing the so-called terminal velocity.

$$v^2 = \frac{2V_p g(\rho_p - \rho_l)}{C_D\rho_l A_p} \qquad (12)$$

While it is straightforward to predict the terminal velocity of the β-phase particle knowing the observed averaged diameter from the micrographs, it does not actually help to understand the complexity behind the settling phenomenon. The morphology of the β-phase changes from high surface area flaky type (precipitated from liquid) to coarsened prismatic shape (e.g. comparing fig. 1 with fig. 8) which would decrease both drag coefficient (C_D) and projected area (A) drastically causing gradual increase in the terminal velocity. Thus, assuming spherical β-phase of 10μm diameter the obtained velocity of about 4×10^{-5} m/s could only be considered, at best, as the highest ceiling value for the terminal velocity at the end of the coarsening phenomenon.

It is important to note that below eutectic temperature the equilibrium amount of β-phase is same for both 6Si and 10Si alloys (6.4% mole/mole which translates to 5.2% V/V

considering the density of β-phase as 3460 kg/m^3) as per the results obtained from the thermodynamic calculations (e.g. fig. 6 (c)). Though the equilibrium volume fraction of β-phase at or below the eutectic temperature is about 5.2%, the image analysis results show that the area fraction of β-phase is about 9.3% in as-cast sample. Such apparent discrepancy between area and volume fraction lies in the fact that the area fraction is always higher than the volume fraction even for an ideally random distribution of spherical particles; such deviation is even more for complex shaped particles as discussed in details in literature [23].

4.3 Morphological change of β-phase

The strategy of gravitational segregation would not be so useful for 6Si alloy since liquid-intermetallic two-phase equilibrium can exist only above 620 ^{o}C and at that temperature phase fraction of intermetallic phase (α-phase) would be rather small (about 1.2%), as can be seen from fig. 6 (a), which is less than half when compared to 3.6% for 10Si (at 600 ^{o}C). Therefore, for any real application Fe removal by gravity segregation of alpha-phase in 6Si would seem to be less effective. On the other hand, gravitational segregation of β-phase in 6Si alloy at lower temperature, say at 600 ^{o}C, would cause hindered settling (of β-phase) due to the presence of the pro-eutectic Al dendrites. This would cause less clear macroscopic demarcation between the liquid and β-phase. Therefore, on a safer side it could be said that iron removal through gravitational segregation of β-phase is better suited for high silicon (near eutectic composition) Al-Si alloy where pro-eutectic Al is less.

As mentioned earlier, during the segregation of β-phase its morphological change was also observed in liquid-solid two-phase equilibrium; in addition to that, it is well known that solid-solid interfacial energy is always higher than the solid-liquid interfacial energy. Therefore, it was natural to expect that to minimise the interfacial energy, the morphological change of the β-phase could be brought about by using suitable heat-treatment in solid-state as well. Accordingly, both 6Si and 10Si samples were isothermally held at 572 ^{o}C for 24 hour. The

idea behind this heat treatment is to go to a temperature as high as possible near to the eutectic point (575.7 ^{o}C) to facilitate faster diffusion of the chemical species and thereby facilitating faster change in the morphology of the β-phase. The microstructures of these samples are shown in fig. 10 (a) and (b) for 6Si and 10Si, respectively. As the amount of β-phase is almost identical in both 6Si and 10Si alloy samples and the microstructure is also appeared to be similar. Upon comparison with the as-cast sample (fig. 1) it becomes rather clear that the platelets of β-phase get refined by fragmentation. In fact, image analysis results on 10Si sample reveal that the average aspect ratio of β-phase platelets reduces from 6.2 to 2.7 from as-cast to the one isothermally held at 572 ^{o}C for 24 hour (fig. 7 (b)). It is equally interesting to observe that the Si particles also tend to be more spheroidized as indicated in fig. 10 (c); and subsequent x-ray mapping clearly demonstrate that the grey-shaded rounded particles almost obscured in the background (Al matrix) are nothing but Si particles; as evident from fig. 11 (a-c). Therefore, it could be considered that the as-cast microstructures of the 6Si or 10Si alloys are actually far from the equilibrium.

It has also been thought to modify the morphology of the β-phase just above the eutectic temperature, at 580 ^{o}C, but without inducing any segregation. Accordingly, only 2 hour of soaking was given to 6Si and 10Si samples at 580 ^{o}C. From fig. 6 (a) and (b) it could be seen that the phase fractions of the liquid phase are about 38% and 73% at 580 ^{o}C for 6Si and 10Si samples, respectively. As a result, 10Si sample was found distorted after the heat-treatment, however, no visual shape change was observed in 6Si sample. Microstructures for 6Si and 10Si samples aged at 580 ^{o}C are presented in fig. 12 (a-b). The microstructural features are rather identical to that of 10Si sample held at 600 ^{o}C for 2 hour., e.g. fig. 9 (a). Only difference appears between 6Si and 10Si is the amount of liquid phase that finally solidified by eutectic decomposition. So long as morphological changes of β-phase are concerned, one

can compare between fig. 10 and fig. 12 for 6Si and 10Si, respectively. Such comparisons clearly bring forward the following observations –

i. Si content alone does not affect either quantity or shape of β-phase irrespective of the heat treatment condition.

ii. Change in morphology of β-phase is strongly dependent on the heat-treatment temperature. Aging above eutectic temperature (575.7 ^{o}C) causes faster growth of β-phase (in thickness) due to the faster diffusion in liquid phase [24]; whereas below 575.7 ^{o}C, growth process is slow and fragmentation across the length or along the length is observed.

iii. Morphology of Si particles is also greatly dependent on heat-treatment temperature. Aging below eutectic temperature causes Si lamellae to become spheroidized; but any involvement of eutectic liquid would give rise to zagged-flaky shaped Si resembling to divorced eutectic morphology.

Apart from the above observations regarding the shape of the second phase; fig. 13 (a) shows how eutectic-Si nucleates and grows from a pre-existing β-phase particle in 6Si sample. Similar argument holds true for solidification of 10Si sample, as evident from fig. 13 (b). Based on the observations after aging, it was thought if a combined heat-treatment involving aging at 580 ^{o}C for 2 hour followed by aging at 572 ^{o}C for 24 hour would result in better mechanical properties. Accordingly, this heat-treatment was carried out only for 6Si samples. The tensile stress-strain curves of 6Si specimen with different heat-treated conditions are presented in fig. 14 alongside with the as-cast specimen. From the figure, it is evident that the long-term aging at 572 ^{o}C indeed causes improvement in ductility with marginal loss in strength and yield strength. Tensile properties derived from the stress-strain curves are given in table 3. It is imperative that one can optimize the time and temperature in order to achieve a best compromise between the strength and ductility. This is also interesting to note the

serrated plastic flow in the aged sample due to dynamic strain aging (DSA), which is also known as Portevin-LeChatelier effect (PLC effect). PLC effect in aluminium alloy due to dynamic strain aging is a known phenomenon and is reported in literature [25].

The correlations between the heat-treatment and corresponding morphology of the phases as well as the tensile properties appear to be straightforward. Improvement of the tensile properties strongly depends on the elimination of stress concentrating features (i.e. shape of existing β-phase or eutectic Si producing sharp corners) in high Fe bearing Al-Si alloy. Aging for prolonged time below eutectic point rounded-off the existing eutectic Si phase and β-phase to a lesser extent causing improvement in ductility; however, grain growth causes reduction in 0.2% offset yield strength and UTS. It is interesting to note that holding for shorter period slightly above eutectic temperature does not exhibit better tensile properties than that of as-cast structure despite the fact that β-phase grows and sharp edges are eliminated. This could be reasoned by considering the facts that upon solidification, the Si morphology gives rise to zagged flaky shape with sharp corners (e.g. fig. 12 (a) or fig. 13 (a)) and at the same time, average grain size increases as well; thus reducing both ductility and strength. However, best result is obtained when it is again subjected to solid-state aging below eutectic temperature causing rounding off the eutectic Si alongwith the rounded β-phase. In any case best yield strength is obtained in as-cast condition due to lower grain size. It is to be emphasized that there is a scope of optimization in terms of aging temperature and time to obtain the best possible combination of the tensile properties.

4.4 Mechanism of morphological change

It could be seen from fig. 1 (b) that the primary β-phase platelets are of high aspect ratio when form above eutectic temperature. Such high aspect ratio is expected due to crystallographically anisotropic growth while precipitating from the liquid phase for faster accommodation of atoms across the liquid-beta interface during solidification. As a result, the

as-cast microstructure is in metastable state due to high surface area of the primary β-phase platelets. In order to minimize the surface energy two conditions must be satisfied simultaneously; microscopically the lowest energy crystallographic interface should prevail and macroscopically, surface area of β-phase platelet should be minimized [26]. Thus, during aging a dynamic equilibrium can be conceived, where atoms from β-phase diffused into matrix and precipitates again on the existing β-phase platelets satisfying these two conditions and thus minimizing the surface energy as well as the aspect ratio. Naturally, minimization of surface energy in this case would be a diffusion-controlled phenomenon and aging at higher temperature or involvement of liquid matrix would accelerate this process due to enhanced diffusivity. On the other hand, aging in solid-state condition would take longer time in order to achieve the low energy morphology due to lower diffusivity. Further, involvement of liquid phase would also cause rapid growth of the β-phase possibly by Ostwald ripening.

It is to be noted that, β-phase always inherits longitudinal and transverse cracks as shown in Fig. 2 (a- b) and/or in fig. 13 (b); which is also studied in details and reported in the literature [27]. Presence of cracks and fragmentation of the beta phase has also been observed by the other researchers in Al- 12 wt% Si alloy [28] and Al- 9 wt% Si alloy [29] when heat treatment below eutectic temperature was carried out. Such cracks provide additional high-energy surface area through which atomic diffusion could take place and eventually the platelets would appear in fragmented-yet-aligned morphology in the microstructure, as shown in fig. 10 (c). In addition, the thickness of the fragmented platelets should increase upon aging resulting in lower aspect ratio and round-edged particle as evident from fig. 7 (b) and fig. 10, respectively. This phenomenon is depicted in fig. 15 in a self-explained manner.

5. Conclusions

From the foregoing discussion the following concluding points could be drawn –

i. General philosophy of managing high Fe content in recycled Al-Si alloys has been discussed and two potential methods for engineering β-phase have been identified; i.e. gravitational segregation and morphological change.

ii. With the help of thermodynamic calculations it was found out that below about 0.5wt% Si, β-phase can not be formed irrespective of Fe concentration. For a given Fe concentration, yield of β-phase is independent of Si content above a threshold Si concentration and these interrelationships have been expressed using mathematical inequalities.

iii. Morphological change of β-phase (via suitable heat-treatment) in low-Si high-Fe content recyclable Al-Si alloy is preferred choice to counteract the detrimental effect of Fe content. On the other hand, elimination of Fe via gravity segregation of β-phase is ideal method for high-Si content alloy.

iv. Fragmentation theory has been proposed as the chief mechanism for the refinement of primary β-phase upon solid-state aging based on the experimental evidences; such solid-state refinement also exhibits better tensile properties.

v. Step-aging above and below eutectic point results into better tensile properties in 6Si alloy due to spheroidization of both β-phase and Si particles.

Acknowledgment

The authors acknowledge that the present work has been carried out under the aegis of Marie Sklodowska Curie Individual Fellowship (MSCA-IF-2015), European Commission (EU project no. 656943).

References

1. J. A. S Green (ed), Aluminum recycling and processing for energy conservation and sustainability, ASM International, US (2007)
2. C. Schmitz (ed), Handbook of aluminium recycling, Vulkan Verlag, Germany (2006)
3. G. Gaustad, E. Olivetti, R. Kirchain, Improving aluminum recycling: A survey of sorting and impurity removal technologies, Resour. Conserv. Recycl 58 (2012) 79

4. V.G. Rivlin, G.V. Raynor: Int. Met. Rev.,26 (1981) 133
5. G. Ghosh, Ternary Alloys Vol. 5, G. Petzow and G. Effenberg (eds.), VCH Publishers, Germany, (1992) 394
6. N. Krendelsberger, F. Weitzer, J. C. Schuster, On the reaction scheme and liquidus surface in the ternary system Al-Fe-Si, Met. Mat. Trans. A, 38A (2007) 1681
7. M. C. J. Marker, B. Skolyszewska-Kühberger, H. S. Effenberger, C. Schmetterer, K. W. Richter, Phase equilibria and structural investigations in the system Al-Fe-Si, Intermetallics, 19 (2011) 1919
8. A. Gorny, J. Manickaraj, Z. Cai, S Shankar, Evolution of Fe based intermetallic phases in Al–Si hypoeutectic casting alloys: Influence of the Si and Fe concentrations, and solidification rate, J. Alloy Com. 577 (2013) 103
9. J. A. Taylor, Iron-containing intermetallic phases in Al-Si based casting alloys, Proc. Mat. Sci. 1 (2012) 19
10. C. M. Dinnis, J. A. Taylor, A. K. Dahle, As-cast morphology of iron-intermetallics in Al–Si foundry alloys, Scripta. Mater., 53 (2005) 955
11. S.G. Shabestari, The effect of iron and manganese on the formation of intermetallic compounds in aluminum–silicon alloys, Mat. Sci. Eng. A 383 (2004) 289
12. E. Taghaddos, M.M. Hejazi, R. Taghiabadi, S.G. Shabestari, Effect of iron-intermetallics on the fluidity of 413 aluminum alloy, J. Alloy. Comp. 468 (2009) 539
13. Unpublished results
14. N.A. Belov, A.A. Aksenov, D. G. Eskin, Iron in aluminium alloys: impurity and alloying element, Taylor & Francis Inc, New York (2002)
15. H. L. de Moraes, J. R. de Oliveira, D. C. R. Espinosa, J. A. S. Tenorio, Removal of iron from molten recycled aluminum through intermediate phase filtration, Mater. Tran. 47(7) (2006) 1731
16. S. L. Chen, F. Zhang, F. Y. Xie, S. Daniel, X. Y. Yan, Y. A. Chang, R. Schmid-Fetzer, W. A. Oates, Calculating phase diagram using PandaT and Panengine, JOM, vol. 55, no. 12 (2003) 48
17. W. S. Rasband, ImageJ, U. S. National Institutes of Health, Bethesda, Maryland, USA, http://imagej.nih.gov/ij/, 1997-2015
18. ASTM B557-10, Standard Test Methods for Tension Testing wrought and cast aluminium and magnesium alloy product, ASTM International, West Conshohocken, PA, 2015, www.astm.org
19. A. T. Dinsdale, SGTE Data for Pure Elements, CALPHAD, 15(4) (1991) 317
20. U. R. Kattner, The thermodynamic modeling of multicomponent phase equilibria, 49 (12) (1997) 14
21. A. Verma, S. Kumar, P.S. Grant, K.A.Q. O'Reilly, Influence of cooling rate on the Fe intermetallic formation in an AA6063 Al alloy, J. Alloy. Comp. 555 (2013) 274
22. S. G. Shabestari, J. E. Gruzleski, Gravity segregation of complex intermetallic compounds in liquid aluminum-silicon alloys, Met. Mat. Trans. A 26 (4) (1995) 999
23. C. B. Basak, A. K. Sengupta, Development of a FDM based code to determine the 3-D size distribution of homogeneously dispersed spherical second phase from microstructure: a case study on nodular cast iron, Scripta Mat. 51 (3) (2004) 255
24. J. Wang, P. D. Lee, R. W. Hamilton, M. Li, J. Allison, The kinetics of Fe-rich intermetallic formation in aluminium alloys: In situ observation, Scripta Mat. 60(7) (2009) 516
25. K. Peng, W. Chen, K. Qian, Study on dynamic strain aging phenomenon of 3004 aluminum alloy, Mat. Sci. Eng. A, 415 (1–2) (2006) 53
26. C. B. Basak, Microstructural evaluation of U-rich U-Zr alloys under near-equilibrium condition, J. Nucl. Mat. 416 (3) (2011) 280
27. X. Cao, J. Campbell, Morphology of β-Al_5FeSi Phase in Al-Si Cast Alloys, Mater. Tran. 47(5) (2006) 1303
28. C. Villeneuve, F. H. Samuel, Fragmentation and dissolution of β-Al_5FeSi phase during solution heat treatment of Al-Si-Fe alloys, Int. J. Cast Metals Res. 12 (1999) 145
29. A. Eshaghi, H.M. Ghasemi, J. Rassizadehghani, Effect of heat treatment on microstructure and wear behavior of Al-Si alloys with various iron contents, Materials and Design 32 (2011) 1520

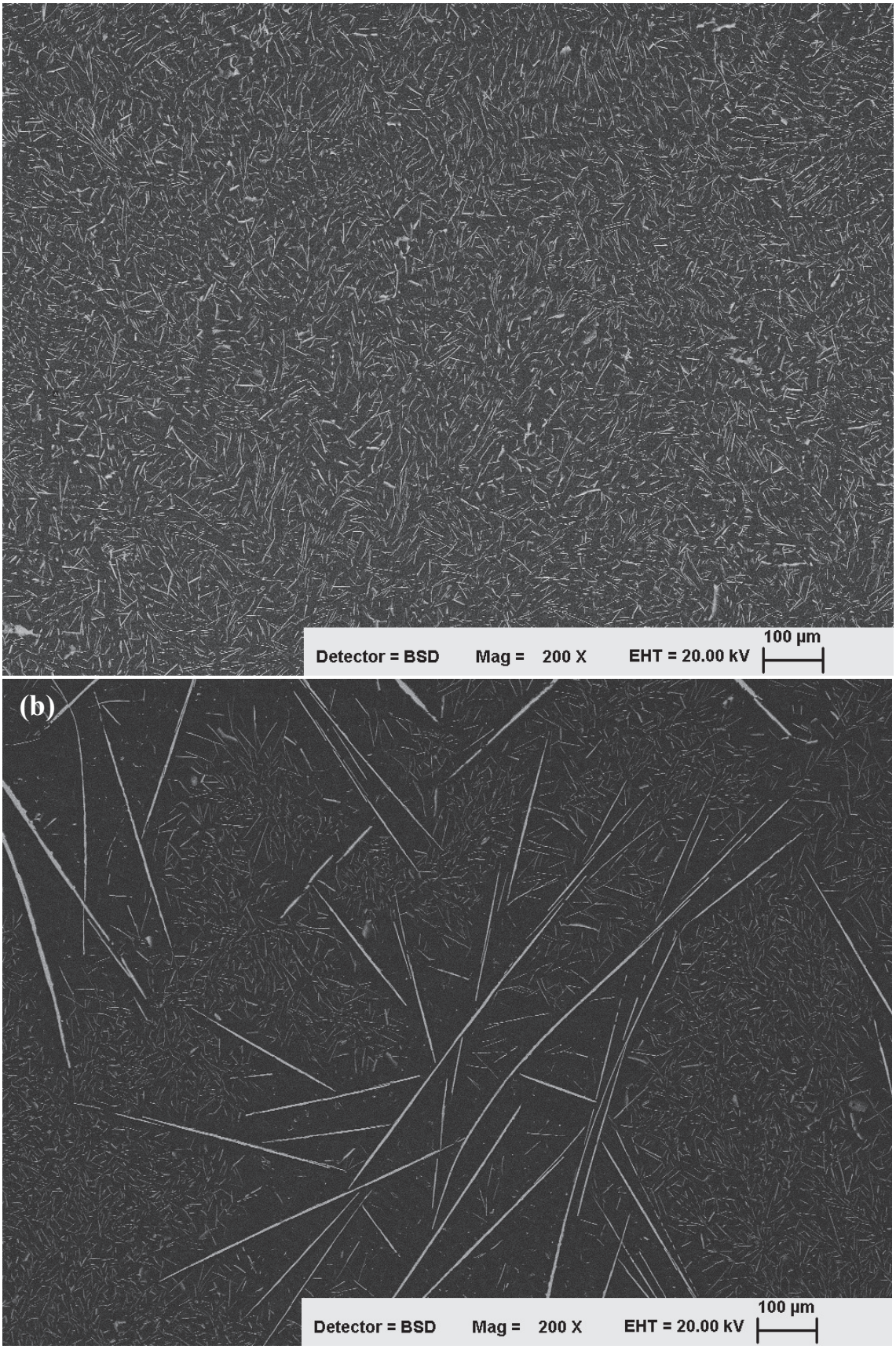

Figure 1. BSE (back scattered electron) micrograph of (a) 6Si (near edge) and (b) 10Si (near center) samples in as-cast condition, white β-phase is clearly visible in dark Al background which also contains eutectic colonies (not visible in BSE)

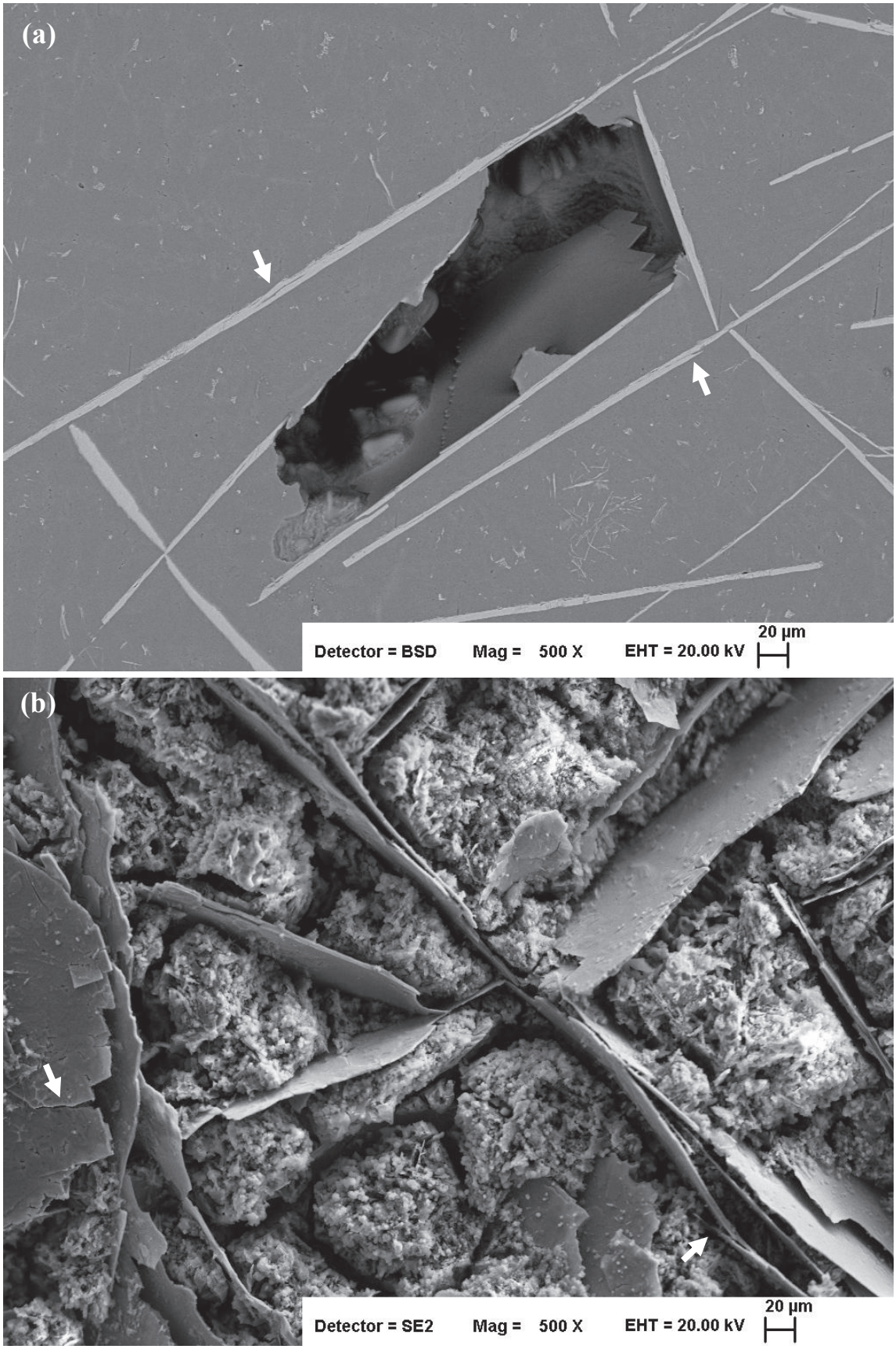

Figure 2. Micrograph of 10Si sample showing (a) shrinkage porosity caused by β-phase and (b) complex morphology of plate shaped β-phase in deep etched sample. Arrows indicate pre-existing cracks in the β-phase platelets.

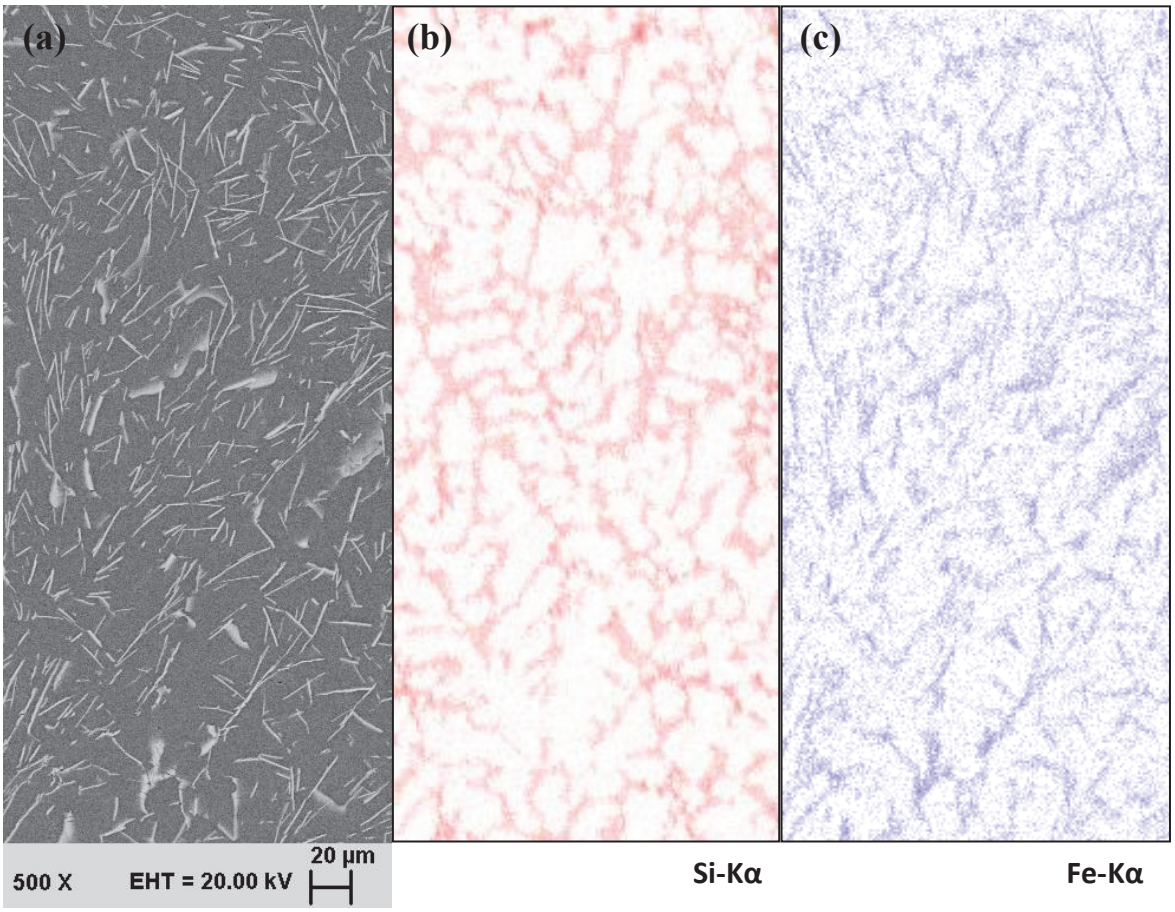

Figure 3. (a) BSE micrograph of as-cast 6Si sample alongwith corresponding x-ray mapping showing (b) eutectic Si and (c) Fe in β-$Al_9Fe_2Si_2$ phase using Si-K_α and Fe-K_α characteristics x-ray.

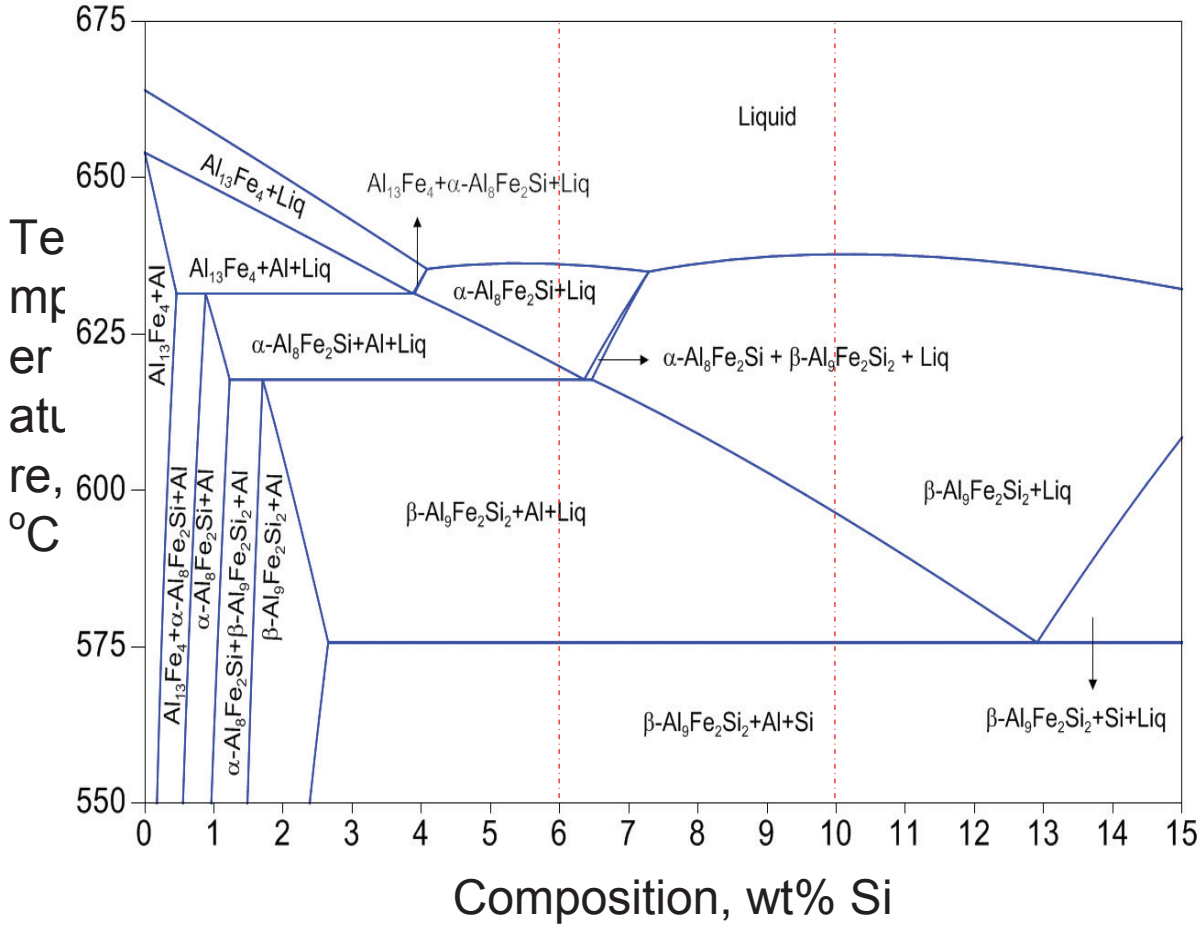

Figure 4. Isopleth of Al-Fe-Si system sectioned at 2 wt% Fe, red dashed lines indicate 6 wt% and 10 wt% Si compositions.

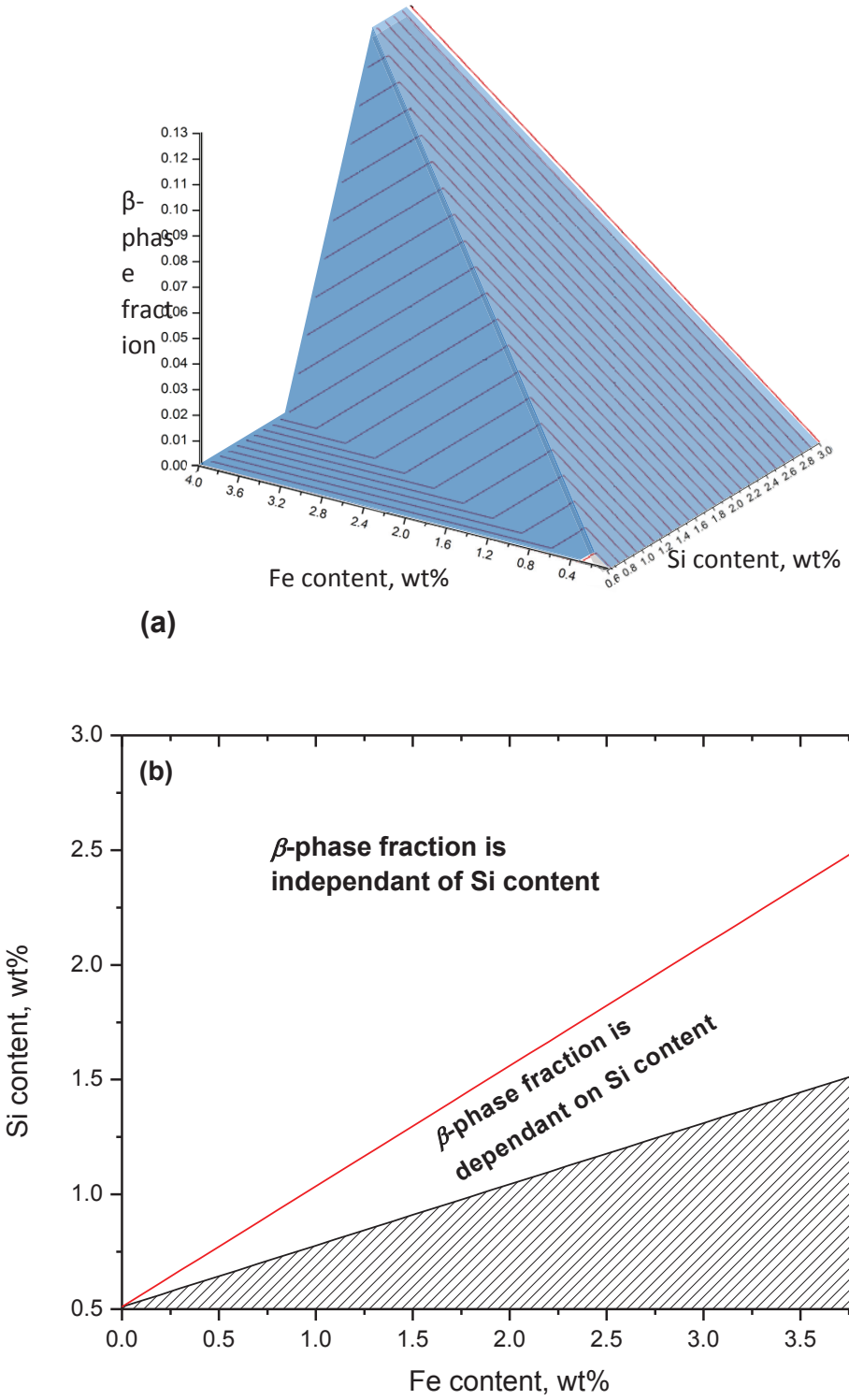

Figure 5. CALPHAD results of (a) yield of β-phase (mole/mole) at eutectic point (575.6 ^{o}C) as a function of Si (0.6 to 3 wt%) and Fe (0 to 4 wt%) content. (b) The projection of β-phase yield at 575.46 ^{o}C in compositional plane showing three distinct regions; the shaded region is where formation of β-phase is thermodynamically prohibited. Also, it is interesting to note that below about 0.5 wt% Si, β-phase can not be formed irrespective of Fe concentration.

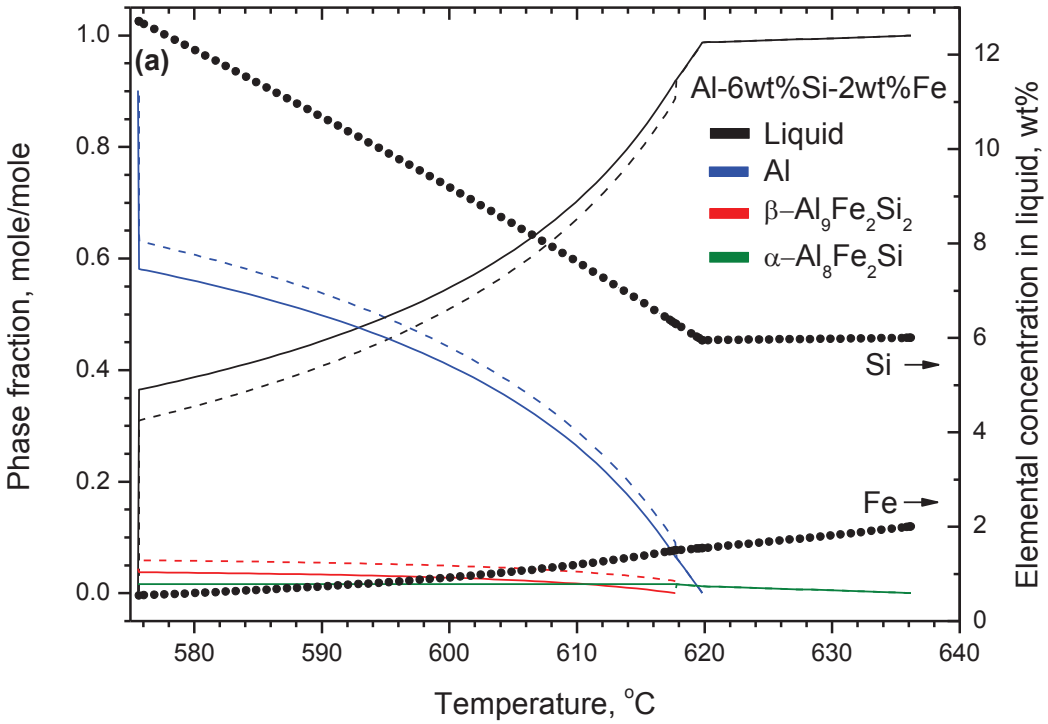
(a)
Al-6wt%Si-2wt%Fe
Liquid
Al
β–Al9Fe2Si2
α–Al8Fe2Si
Si
Fe
Phase fraction, mole/mole
Elemental concentration in liquid, wt%
Temperature, °C
1.0
0.8
0.6
0.4
0.2
0.0
12
10
8
6
4
2
0
580
590
600
610
620
630
640

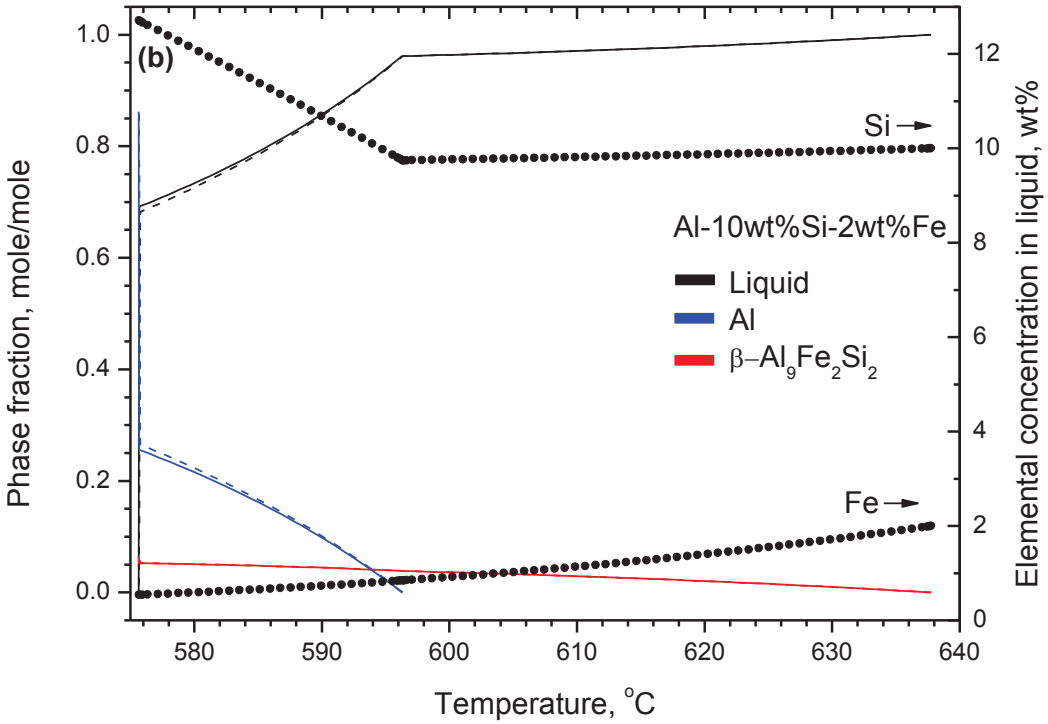
(b)
Si
Al-10wt%Si-2wt%Fe
Liquid
Al
β–Al9Fe2Si2
Fe
Phase fraction, mole/mole
Elemental concentration in liquid, wt%
Temperature, °C
1.0
0.8
0.6
0.4
0.2
0.0
12
10
8
6
4
2
0
580
590
600
610
620
630
640

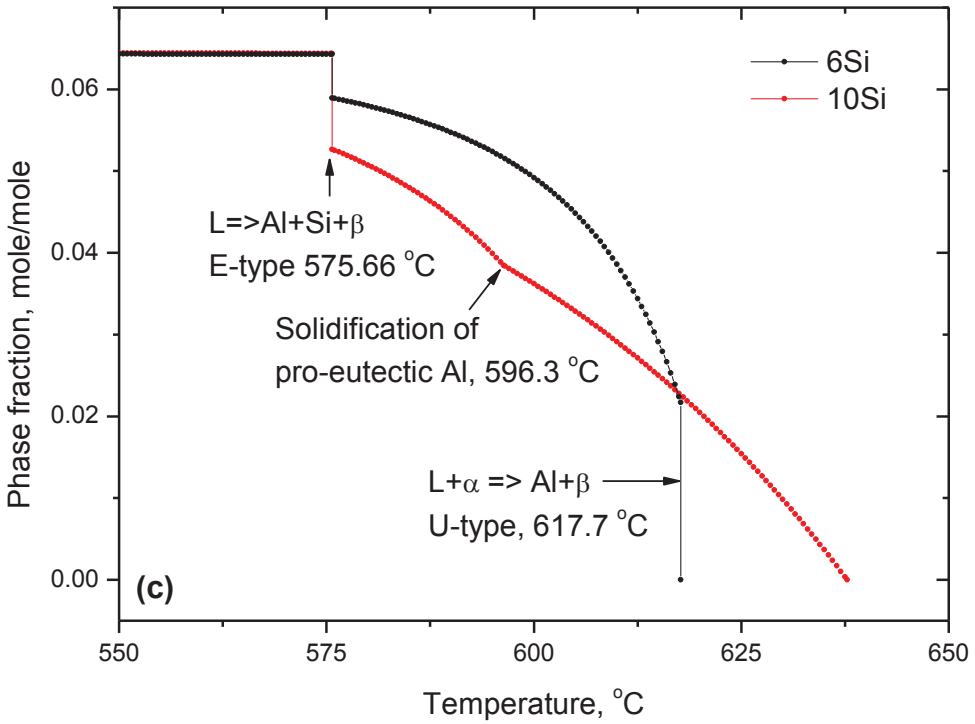

Figure 6. Simulation of solidification as per equilibrium model and Scheil model for (a) 6Si and (b) 10Si alloys. Solid line indicates Scheil model of solidification whereas dashed line indicates lever rule method (equilibrium model). Symbol+line (right hand axis) are for the composition of the liquid phase. Note that liquid composition profile does not change from eqilibrium model to Scheil model. (c) Yield of β-phase as a function of temperature for both 6Si and 10Si.

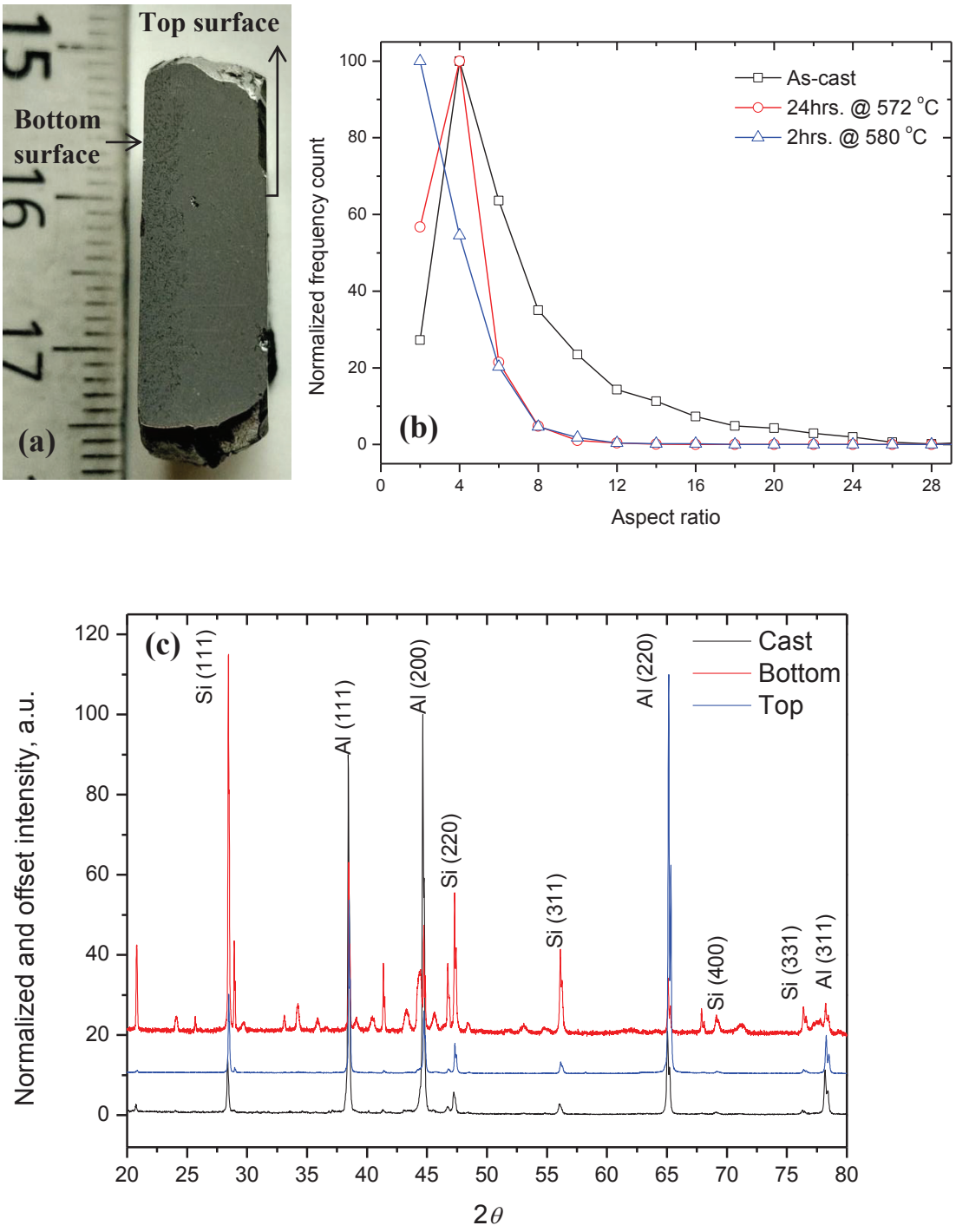

Figure 7. (a) Macrophotograph of visible gravitational segregation of β-phase after exposing 10Si sample to 600 °C for 2 hour (minimum scale division is 1 mm). (b) Normalized frequency count of the aspect ratio of β-phase needles as obtained from the image analysis results. (c) XRD trace from top and bottom surface of the same sample and compared with as-cast sample; showing strong presence of β-phase (all unlabelled peaks) and Si particles with strong (111) peaks alongwith fcc aluminium from the bottom surface. Both as-cast and top surface exhibits negligible amount of β-phase. However, prevalence of (220) planes and (200) planes of Al is the characteristics of the top surface and as-cast sample respectively.

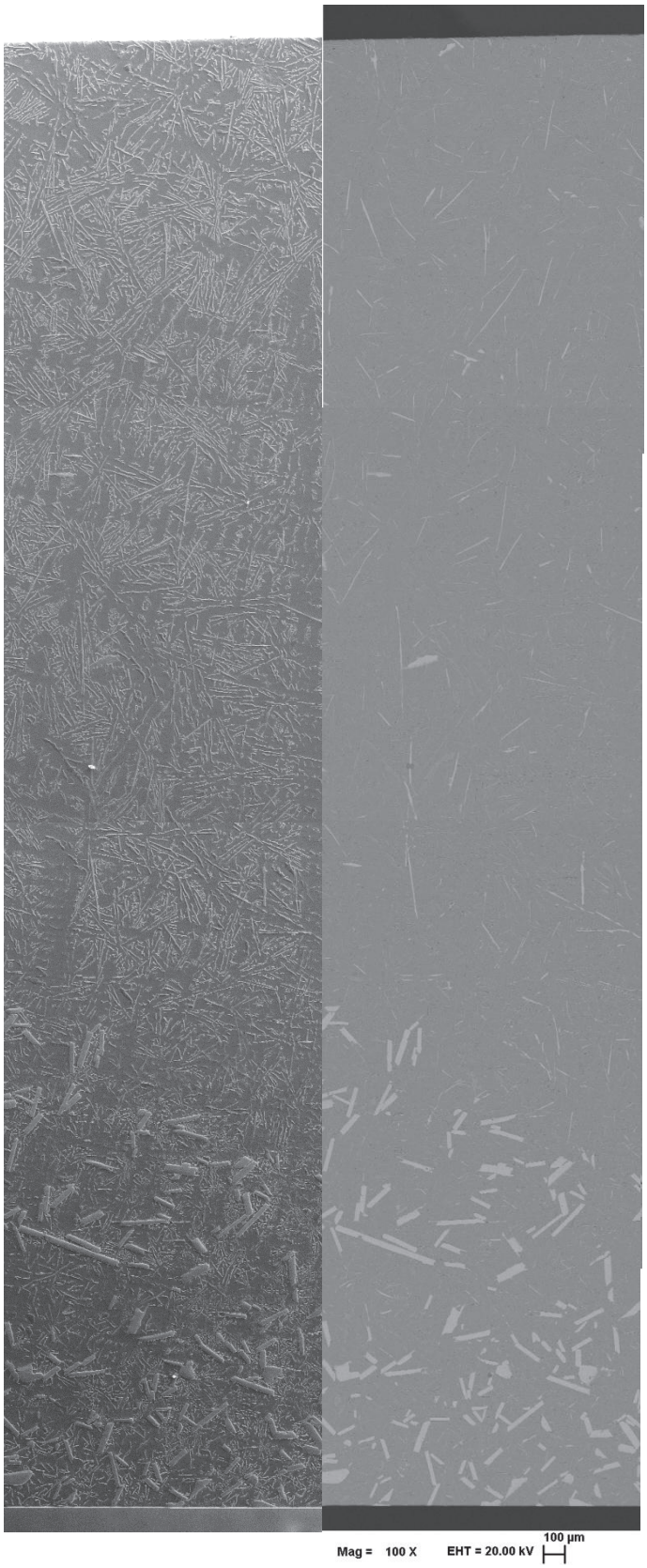

Figure 8. Stitched photomicrographs of 10Si sample heat treated at 600 ^{o}C for 2 hour showing gravitational segregation of β-$Al_9Fe_2Si_2$ phase. Left part of the micrograph is secondary electron image showing both Si and β-$Al_9Fe_2Si_2$ phase; whereas BSE (right part) contrast of the same area is only due to Fe showing β-$Al_9Fe_2Si_2$ particles.

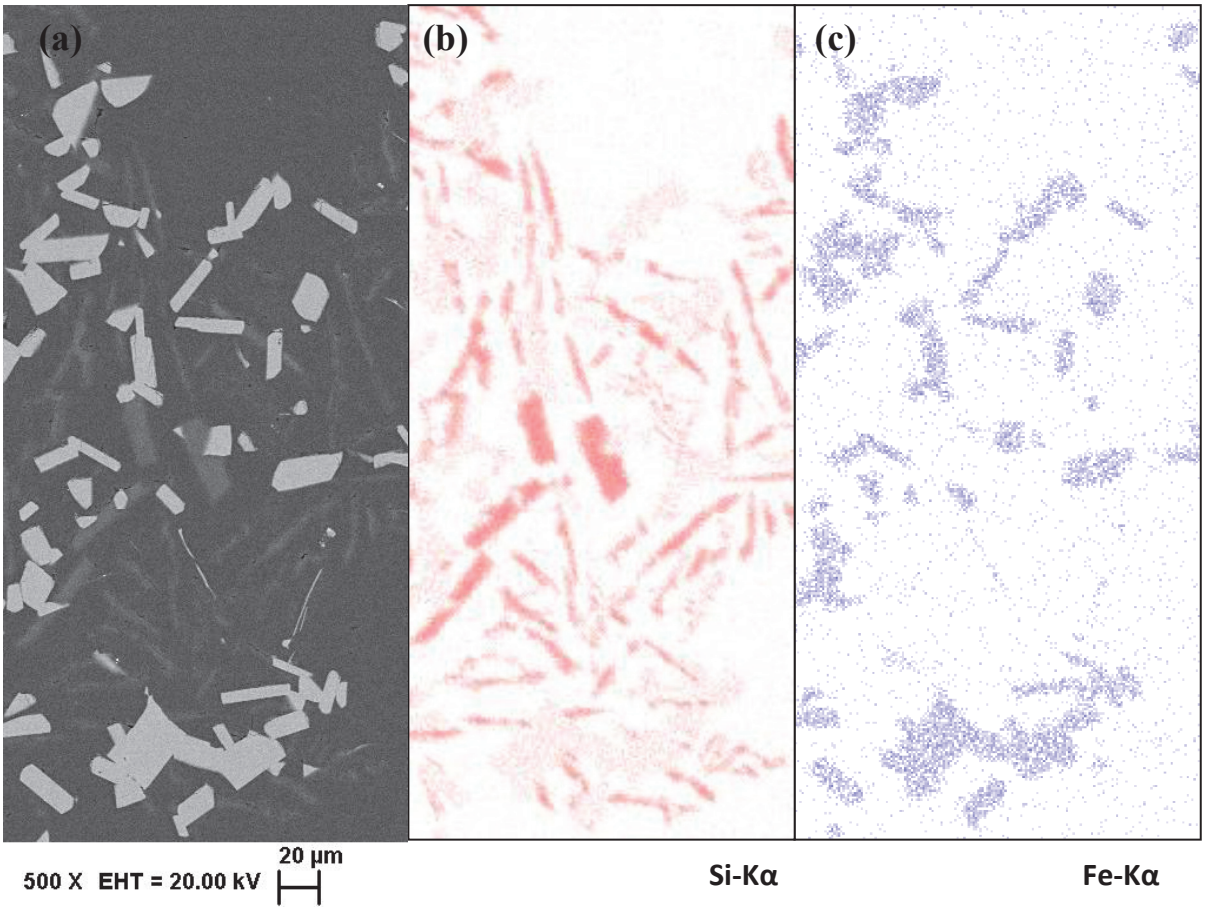

Figure 9. (a) BSE micrograph of segregated 10Si sample (bottom surface) isothermally held at 600 ^{o}C for 2 hour alongwith corresponding x-ray mapping showing (b) Si in divorced eutectic and (c) Fe in β-$Al_9Fe_2Si_2$ phase.

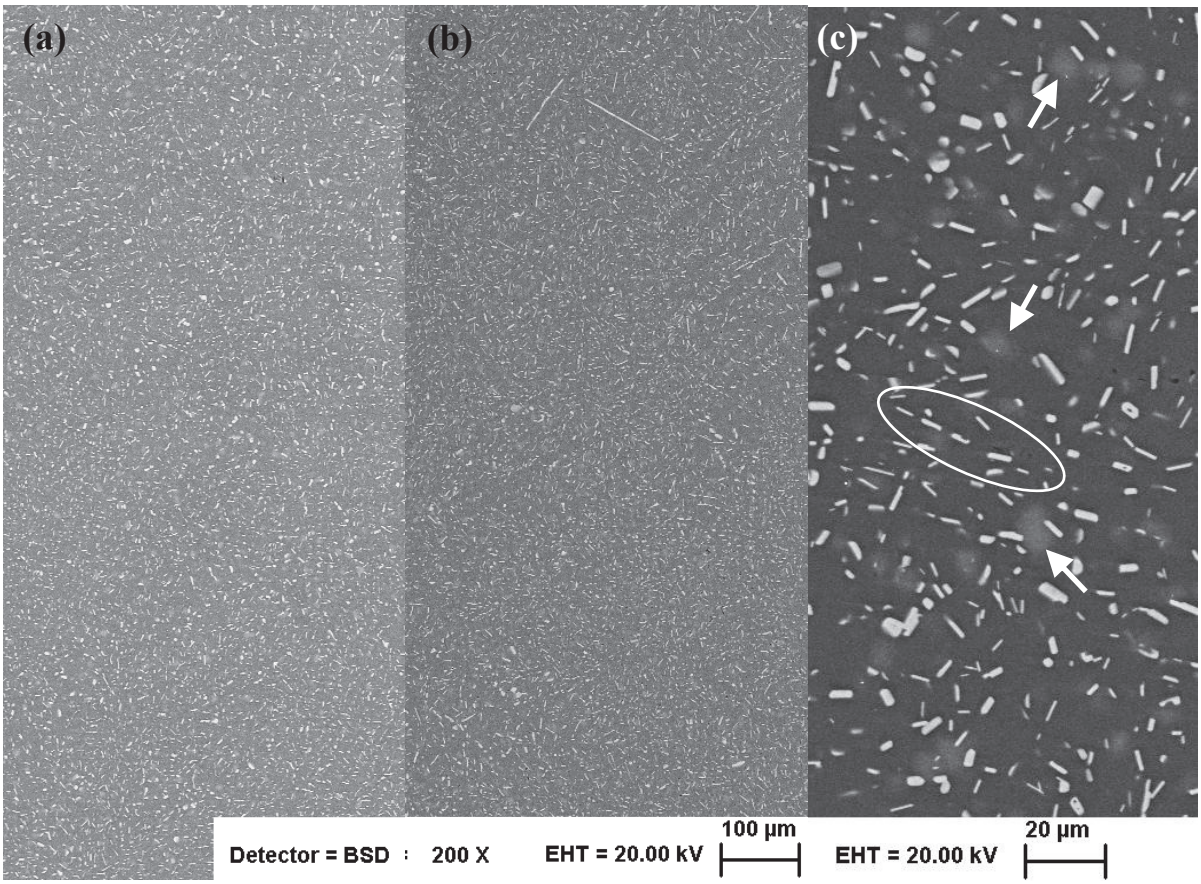

Figure 10. Comparative BSE micrographs of (a) 6Si and (b) 10Si samples isothermally held at 572 ^{o}C for 24 hour. Comparison with figure 1 (a) and (b) reveals remarkable refinement of β-phase. (c) 6Si sample at higher magnification showing fragmented yet aligned β-phase particles (encircled) and rounded Si particles appear as obscure grey features (arrows).

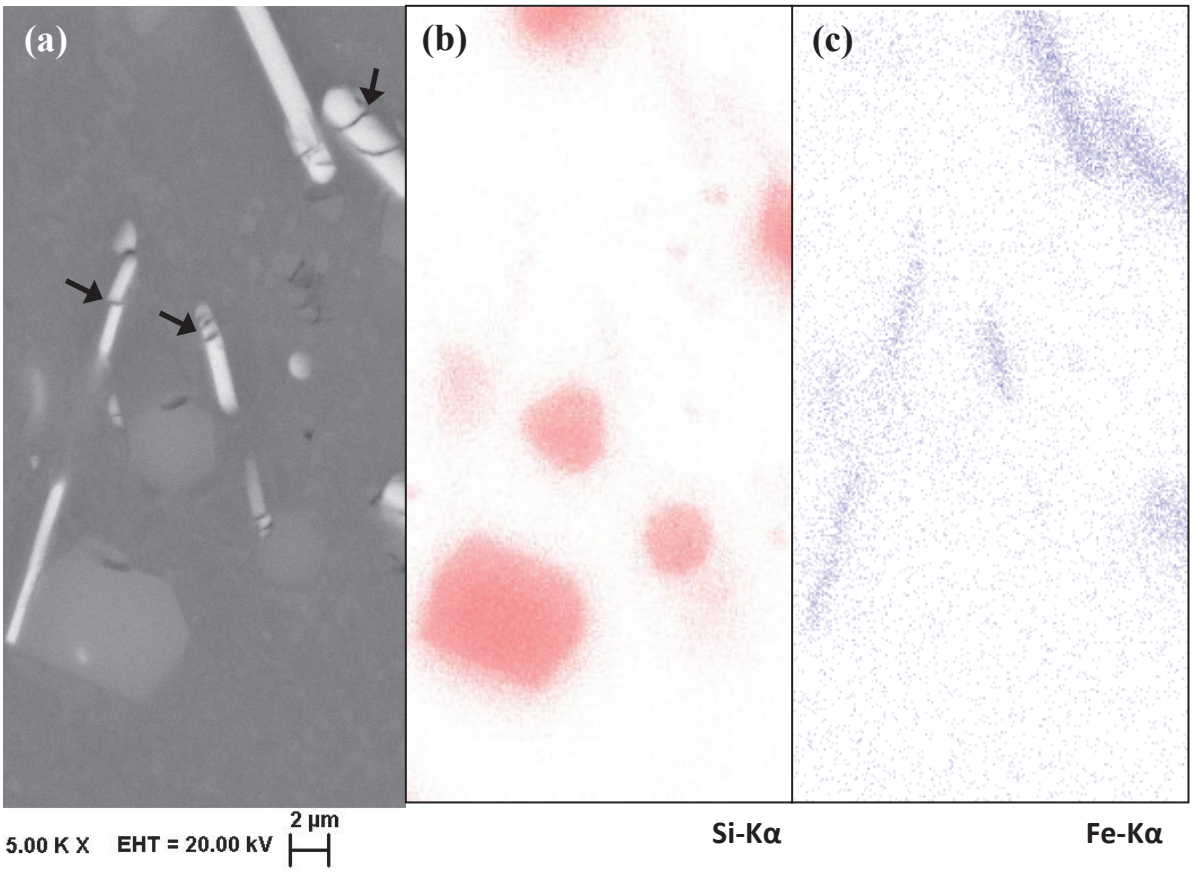

Figure 11. (a) BSE micrograph of 6Si sample (bottom surface) isothermally held at 572 ^{o}C for 24 hour alongwith corresponding x-ray mapping showing (b) rounded blocky Si particles (as shown in fig. 10 c) rather than Si lamellae and (c) Fe in β-phase. Note the cracks/ fragmentation of β-phase indicated by arrows.

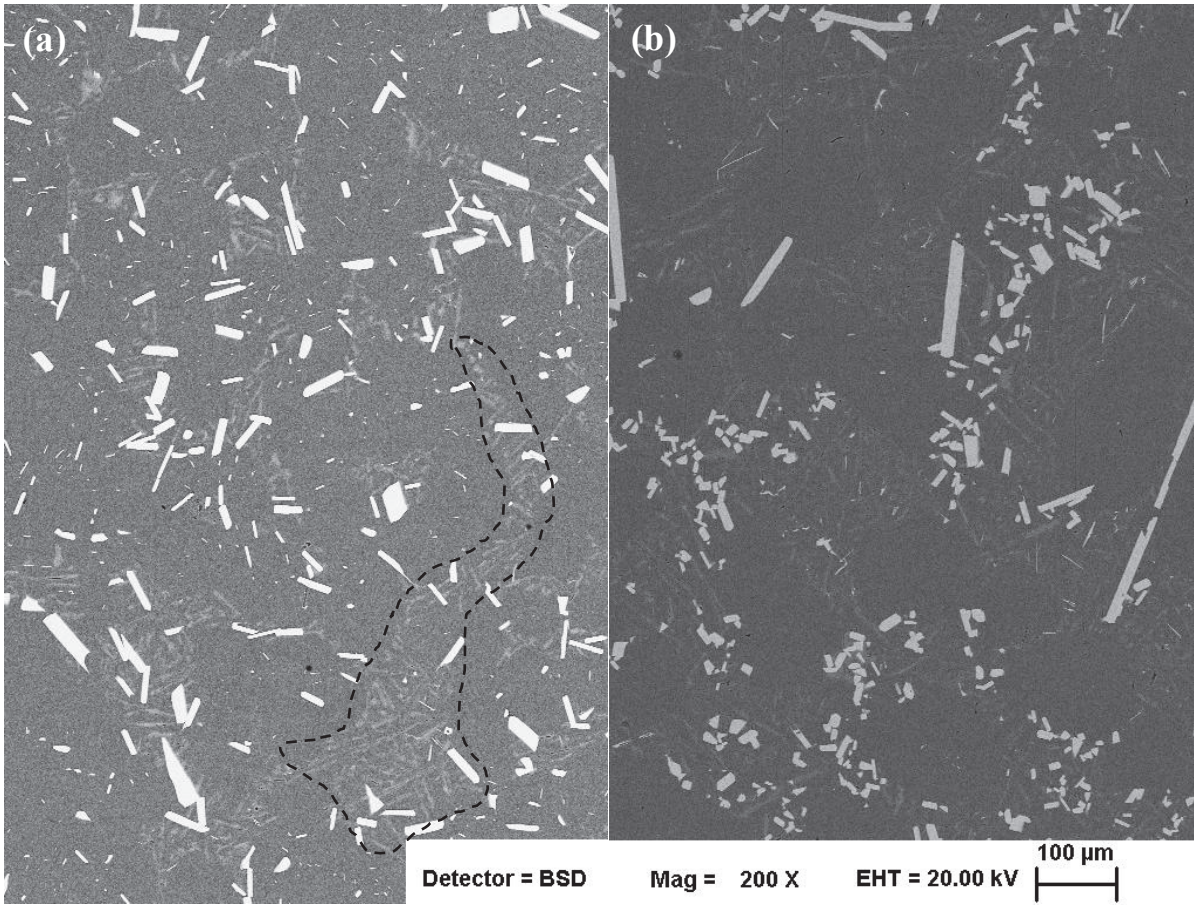

Figure 12. Comparative BSE micrograph of (a) 6Si alloy and (b) 10Si alloy isothermally held at 580 ^{o}C for 2 hour. Note the growth of β-phase platelets and microstructural similarity with figure 9 (a). The Si particles (grey) appear within the network of liquid phase (dashed line) formed during heat-treatment; also note more liquid phase in 10Si sample.

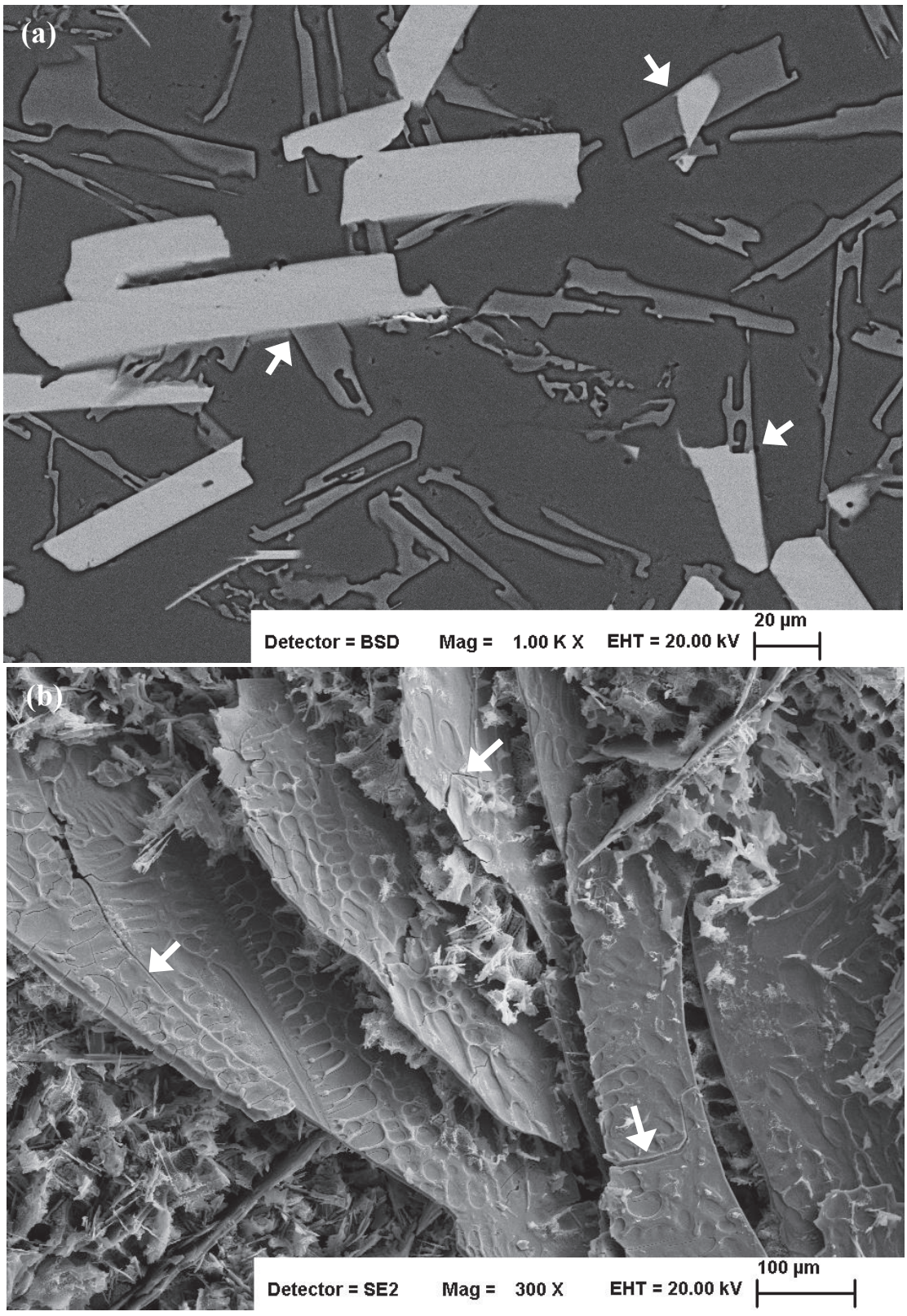

Figure 13. (a) BSE micrograph of 6Si alloy isothermally held at 580 ^{o}C for 2 hour. showing (arrows) growth of Si phase (grey) from existing β-phase (white) upon eutectic solidification. Availability of such preferential nucleation site for Si results into divorced eutectic microstructure. (b) Deep etched 10Si as-cast sample showing growth impression of typical eutectic solidification on the β-phase platelets and arrows indicate existing cracks.

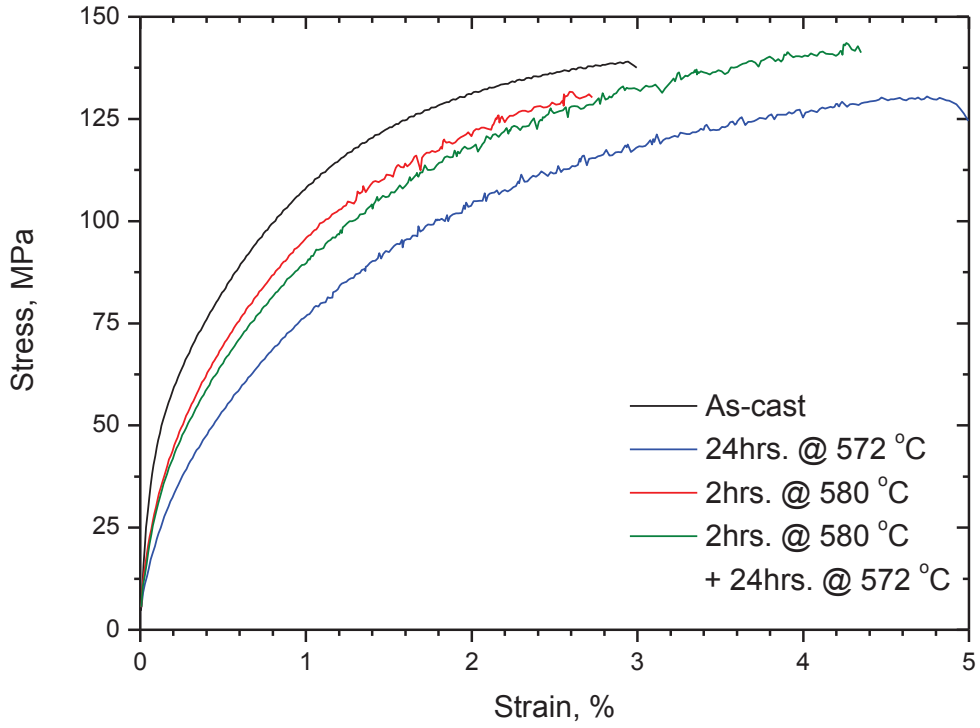

Figure 14: Typical stress-strain curves of 6Si alloy under different heat-treatment conditions; note the serrated plastic flow indicating dynamic strain aging in the heat-treated samples.

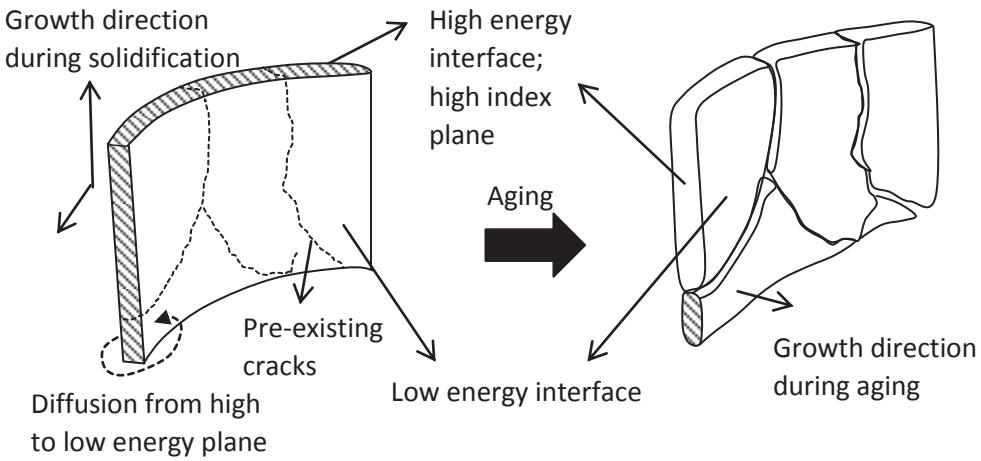

Figure 15. Schematic growth model of primary β-phase platelet during solid-state aging. Shaded surface is the high-index crystallographic plane (for accommodating higher growth speed during solidification) representing high-energy interface and is perpendicular to the direction of solidification. Eventually, the β-phase would appear as fragmented-yet-aligned morphology with rounded edge and lower aspect ratio than their as-cast morphology.

Table 1: Typical chemical composition (in wt%) of 6Si and 10Si samples from GD-OES analysis, elements having concentration less than 0.001 wt% are not shown here. Standard deviation for Si and Fe for 6Si is 0.07 and 0.03; the same for 10Si are 0.12 and 0.04 respectively

Si	Fe	Ga	Ti	In	Mn	Ni	Ca	Sn	Mg	Zn	Cu	P
6.02	**1.97**	0.012	0.011	0.01	0.006	0.006	0.006	0.005	0.004	0.004	0.003	0.002
10.11	**2.06**	0.011	0.013	0.01	0.007	0.007	0.005	0.007	0.005	0.009	0.001	0.002

Table 2: Chemical composition (in at%) of β-phase averaged over 10 random measurements using EDS alongwith standard deviations (σ) in 10Si samples with different heat-treatments

Heat treatment	Al	σ	Fe	σ	Si	σ
As-cast	68.34	0.05	15.92	0.04	15.74	0.01
2 hour @ 600 °C	68.27	0.06	16.18	0.12	15.55	0.05
24 hour @ 600 °C	68.18	0.06	16.52	0.11	15.30	0.12

Table 3: Typical tensile properties of 6Si alloy with different heat-treatment conditions

Heat treatment	Yield stress (0.2%) (MPa)	UTS (MPa)	Elongation (%)
As-cast	70	139.1	2.6
2 hour @ 580 °C	66.5	131.6	2.2
24 hour @ 572 °C	59.8	130.4	3.9
2 hour @ 580 °C then 24 hour @ 572 °C	61.8	143.6	3.8